Protein Cell 2013, 4(8): 598–606
DOI 10.1007/s13238-013-3904-1

Protein & Cell

RESEARCH ARTICLE

Ultrafast, accurate, and robust localization of anisotropic dipoles

Yongdeng Zhang[1,2*], Lusheng Gu[1,2*], Hao Chang[2,3*], Wei Ji[2*], Yan Chen[2,4], Mingshu Zhang[2], Lu Yang[5], Bei Liu[1,2], Liangyi Chen[5]✉, Tao Xu[1,2]✉

[1] College of Life Science and Technology, Huazhong University of Science and Technology, Wuhan 430074, China
[2] National Laboratory of Biomacromolecules, Institute of Biophysics, Chinese Academy of Sciences, Beijing 100101, China
[3] School of Life Sciences, University of Science and Technology of China, Hefei 230026, China
[4] University of Chinese Academy of Sciences, Beijing 100049, China
[5] Laboratory of Cell Secretion and Metabolism, Institute of Molecular Medicine, Peking University, Beijing 100871, China
✉ Correspondence: xutao@ibp.ac.cn (T. Xu), lychen@pku.edu.cn (L. Chen)
Received April 26, 2013 Accepted May 4, 2013

ABSTRACT

The resolution of single molecule localization imaging techniques largely depends on the precision of localization algorithms. However, the commonly used Gaussian function is not appropriate for anisotropic dipoles because it is not the true point spread function. We derived the theoretical point spread function of tilted dipoles with restricted mobility and developed an algorithm based on an artificial neural network for estimating the localization, orientation and mobility of individual dipoles. Compared with fitting-based methods, our algorithm demonstrated ultrafast speed and higher accuracy, reduced sensitivity to defocusing, strong robustness and adaptability, making it an optimal choice for both two-dimensional and three-dimensional super-resolution imaging analysis.

KEYWORDS point spread function, restricted mobility, artificial neural network, super-resolution imaging

INTRODUCTION

When a nanoscale fluorophore is imaged, the collected photons forming the image are distributed following the point spread function (PSF). According to Abbe diffraction limit, the resolution of conventional light microscopy is restricted to approximately $\lambda/2NA$, where λ is the wavelength of emission light and NA is the numerical aperture of the objective (Born and Wolf, 1999). However, one is able to localize isolated emitters with nanometer precision by fitting their images with the PSF (Thompson et al., 2002). This has been exploited in recently developed super-resolution imaging methods, such as photoactivated localization microscopy (PALM) (Betzig et al., 2006), fluorescence (F)PALM (Hess et al., 2006), and stochastic optical reconstruction microscopy (STORM) (Rust et al., 2006).

To improve the resolving power of super-resolution imaging, tremendous efforts have been invested in making probes that emit more photons (McKinney et al., 2009; Chang et al., 2012) and achieve a higher label density (Zhang et al., 2012) or in devising schemes that collect more information from the emitted photons (Shtengel et al., 2009; Aquino et al., 2011). In addition, super-resolution microscopy depends heavily on computational scheme that can accurately extract the localization information from millions of emitters at a high enough speed to be sufficient for real-time data analysis. Commonly, a two-dimensional (2D) Gaussian function has been employed to approximate the true PSF. The Gaussian fit for the photon distribution of a single fluorophore can be optimized by either nonlinear least-squares (NLLSG) (Thompson et al., 2002) or maximum likelihood estimation (MLEG) (Ober et al., 2004; Smith et al., 2010). Despite the wide application of the isotropic Gaussian model in localization microscopy, it is not appropriate for fluorophores with fixed dipole orientations and can introduce systematic errors of tens of nanometers (Enderlein et al., 2006; Stallinga and Rieger, 2010; Engelhardt et al., 2011). This problem has been recently addressed by MLE fitting of the theoretical PSF (MLEwT) of fixed dyes (Mortensen et al., 2010). However, MLEwT is not widely implemented in super-resolution imaging of biological samples, mainly because its low computational speed (0.4 molecule/s) and low convergence rate during fitting.

Moreover, fluorophores in cells may not be fixed but have

*These authors contributed equally to the work.

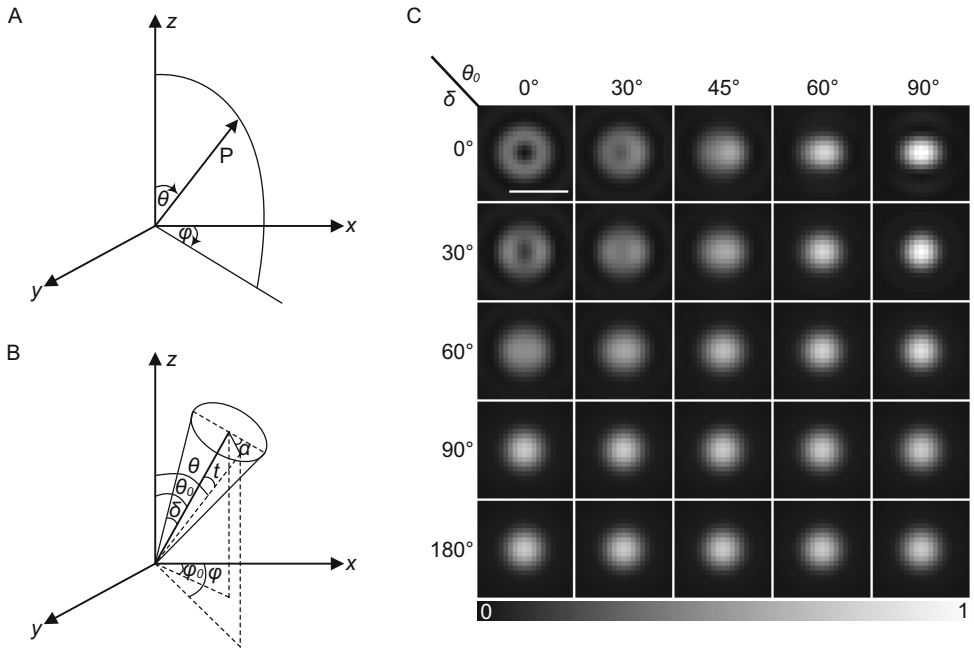

Figure 1. The angular coordinates and emission patterns of dipole. (A) The geometric parameters determining the emission of a fixed dipole P. Here, *z* describes the optical axis. The orientation of a dipole is defined with the azimuthal angle φ and polar angle θ. (B) The geometric parameters determining the emission of a dipole with restricted mobility. The axis of the cone has angular coordinates φ_0 and θ_0. A general orientation in the cone has angular coordinates t and α with respect to the cone axis, where $\alpha = 0°$ is taken at a place in the plane defined by the cone axis and *z*. The outer limit of motion in the cone is given by $t = \delta$. (C) The emission patterns of dipoles with different angular coordinates. Intensity distribution generated by a dipole ($\lambda = 580$ nm) of different θ_0 and δ ($\varphi_0 = 0°$), imaged with a 100 × 1.45 NA objective at a water/glass interface. The pixel size was 40 nm. Scale bar is 500 nm.

different rotational mobility (Testa et al., 2008). The majority of fluorophore dipoles are neither fixed nor free, but in an intermediate state called restricted motion (Dale et al., 1999). Furthermore, even for live cell imaging where the fluorophore is allowed to move freely, it is not clear *a priori* whether the tumbling of the dipole is free enough to give an isotropic emission (Engelhardt et al., 2011). Hence, to maximize the resolving power of super-resolution microscopy, it is important to develop an unbiased estimator with high speed and robustness for dipoles with orientation and restricted motion.

RESULTS

Theoretical PSF of dipoles

First, we considered a dipole oriented with a fixed azimuthal angle φ and polar angle θ (Fig. 1A). The PSF of the fixed dipole can be expressed as previously described (Mortensen et al., 2010). To simplify the case for restricted motion, we supposed that the dipole can rotate around its fixed orientation within a half cone angle δ (Fig. 1B). It is clear that restricted motion is a general model for describing the motion of dipoles, while free ($\delta = 180°$) and fixed ($\delta = 0°$) dipoles are just two special cases of a restricted dipole. In spherical coordinates, it is difficult to derive the PSF of restricted dipoles through numerical integration. Using a special coordinate transformation (Irving, 1996), we were able to find a numerical solution to the PSF of restricted dipoles with different angular coordinates (Fig. 1C).

Artificial neural network

MLE fitting to the theoretical PSF of a dipole is extremely computationally demanding (Mortensen et al., 2010), mainly due to the time required for generating the PSF as well as calculating the log-likelihood for every iteration. Hence, we turn to artificial neural networks (ANNs), which do not require iterative fitting and have been successfully used in biology and chemistry (Cartwright, 2008). The key characteristic of an ANN is its power to approximate any function and to make robust prediction after training with a finite number of discontinuities. This can be particularly useful in single molecule localization, as the true PSF of a dipole is too complicated to fit in a high-throughput fashion.

Experimental validation of ANN algorithm

The basic architecture of an ANN is the mapping between the outputs and inputs (Fig. S1A). Firstly, we followed the framework to train the ANN with synthetic images of dipoles based on theoretical PSFs (Fig. S1B). Next, we validated the trained ANN by comparing its performance with known fitting methods for both isotropic and anisotropic dipoles. For the isotropic

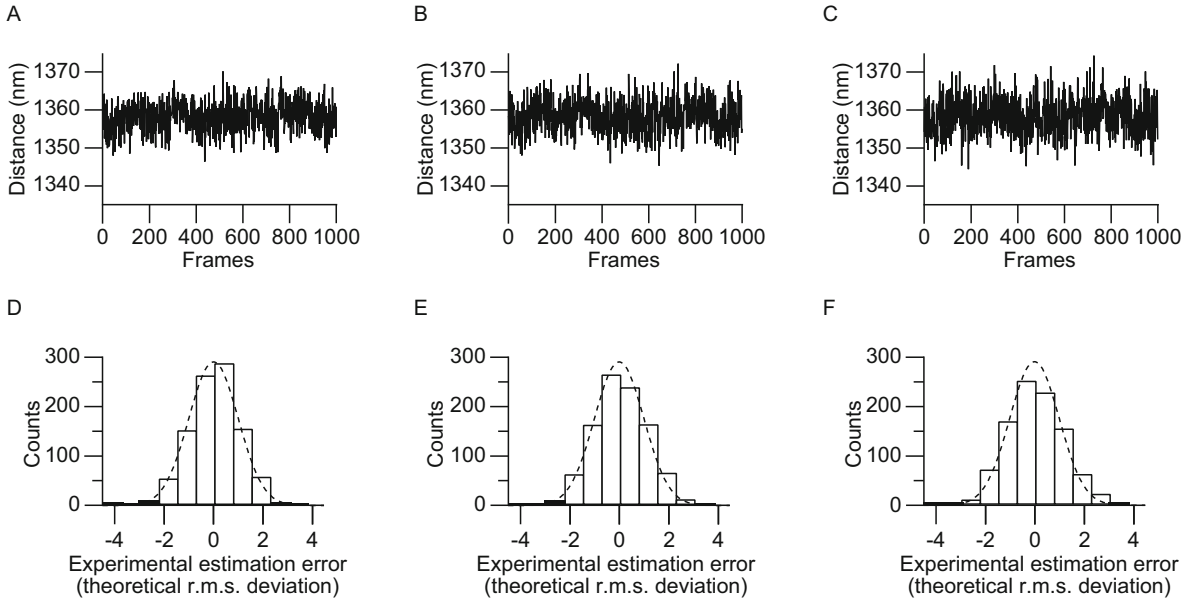

Figure 2. Validation of ANN on isotropic cases. (A–C) The time series of repeatedly measured distances between two fluorescent beads immobilized onto a coverslip obtained with ANN (A), MLEG (B) and NLLSG (C). The mean distances are 1358 nm, 1356 nm and 1359 nm for ANN, MLEG and NLSSG, respectively. The photon numbers of the two beads were 2100 ± 36 and 2209 ± 23 per frame, respectively. (D–F) The histograms of fluctuations about the mean value in the time series of distance estimates with ANN (D), MLEG (E) and NLLSG (F) rescaled by the theoretical r.m.s. deviations. The perfect superimposition of the rescaled fluctuation and normal distribution with unit variance (dashed lines) suggests full agreement between the experimental and theoretical values. The measured standard deviations are 3.79 ± 0.23 nm, 4.20 ± 0.13 nm and 4.57 ± 0.14 nm for ANN, MLEG and NLLSG, respectively.

case, we melted fluorescent beads on a coverslip and estimated the distances between the pairs of beads over a long period of time (Fig. 2A–C). As expected, ANN gave similar estimate as NLLSG and MLEG (Fig. 2D–F). For the anisotropic case of fixed dipoles, we employed quantum rods (Q rods) (Ohmachi et al., 2012), which exhibit linearly polarized emissions, immobilized in a polyacrylamide (PAA) layer. Another consideration of using Q rods is their long lifetime to emit enough photons for multiple-frame imaging, which is required for validating the estimation precision. 4 Q rods of different tilt angles were similarly estimated by ANN and MLEwT (Fig. 3A). We recorded 100 frames for these 4 Q rods and calculated the positions for each frame. The centers and variances of the positions of the first Q rod (θ = 50°) estimated by different algorithms were compared (Fig. 3B). It was evident that positions estimated by ANN and MLEwT were not statistically different from each other, whereas those estimated by MLEG and NLLSG were offset by 12 nm or 16 nm as related to those positions by MLEwT, respectively. The accuracy of localization estimation depended on the polar angle for MLEG and NLLSG. Hence, the more asymmetric of the PSF, the more bias to expect (Fig. 3C). This result is consistent with our simulation where the most asymmetric PSF and the largest bias happen at polar angle around 45° (Fig. S2). In contrast, the position estimation by ANN is not influenced by the orientation (Fig. 3C), confirming that ANN is an unbiased estimator for localization of tilt emitters. Because the ground truth of localization is unknown, it is unclear which of the two estimators, ANN or MLEwT, gives the most accurate estimate. As for the localization precision, we verified that both ANN and MLEwT estimated the localization to the Cramer-Rao lower bound (CRLB) for free, fixed and restricted dipoles, suggesting that ANN-based estimator can reach Fisher's information limit (Fig. S3).

To this point, we have assumed that dipoles were in perfect focus (z = 0). When tilted dipoles are defocused, it has been reported that centroid-based estimators will generate more systematic errors in the localization estimation for up to approximately 100 nm (Stallinga and Rieger, 2010; Engelhardt et al., 2011). We reasoned that by training with defocused PSFs emitted from different z positions (Fig. S4), the ANN method would be able to correct this systematic error and result in higher accuracy in the localization estimation. To validate this, we recorded the images of a Q rod (θ = 36°) at different z positions within ± 300 nm. The centroids of the PSFs were gradually shifted with the increasing z positions, which caused considerable systematic errors (up to 50 nm) in localization estimate by MLEG and NLLSG (Fig. 3D). In contrast, ANN remarkably reduced the systematic error by 5–30 nm (Fig. 3E). As for localization precision, MLEG and NLLSG performed worse at larger z positions because the defocused image is spread over a greater number of pixels, whereas ANN gave consistently better performance at all z positions (Fig. 3F).

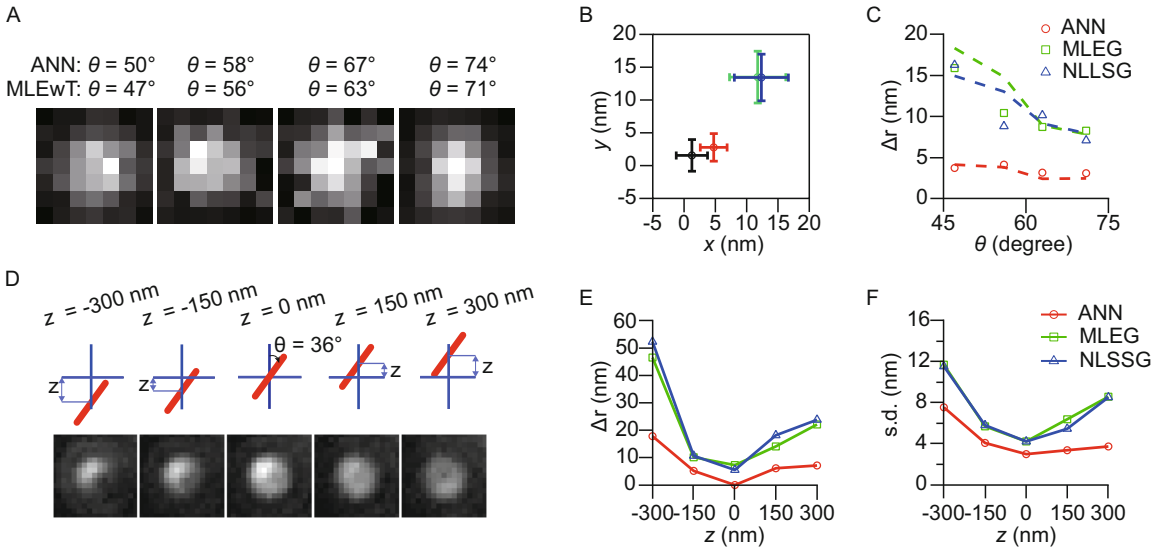

Figure 3. Experimental validation of ANN employing tilted Q rods. (A) Example images of four Q rods with different orientations. The images were estimated by both ANN and MLEwT. The polar angles found were 50 ± 1°, 58 ± 3°, 67 ± 5° and 74 ± 5° for ANN, and 47 ± 1°, 56 ± 3°, 63 ± 4° and 71 ± 4° for MLEwT, respectively. (B) The positions of a Q rod (θ = 47°) obtained by the four algorithms, MLEwT (black), ANN (red), MLEG (green) and NLLSG (blue). 100 frames of images were analyzed. Error bars represent s.d. (C) The relationship of Δr with θ. Here Δr was calculated as the distance between the centroids of positions (calculated from 100 frames) obtained by the three algorithms and that by MLEwT. Dash lines represent simulation results by generating synthetic images with the same parameters (photon, background, orientation) to mimic the Q rods. (D) Examples of a Q rod (θ = 36°) imaged at different *z* positions. (E) The relationship of Δr with *z* positions estimated by three algorithms. Here Δr was referenced to the position at *z* = 0 estimate by ANN. For each *z* position, centroids of positions were calculated from 100 frames. (F) Standard deviation of the positions at each *z* positions estimated by three algorithms.

Evaluating the performance of ANN in super-resolution imaging

To evaluate the performance of ANN in biological samples, we conducted PALM experiments by imaging HeLa cell expressing Lifeact (Riedl et al., 2008) fused with mEos2 proteins (Fig. 4A). We found that proteins exhibited different restricted mobility in fixed cells (Testa et al., 2008) (Fig. S5). To confirm the localization precision of ANN, we selected and analyzed those single molecules with relative longer lifetimes (Fig. 4B). The standard deviation in *x* direction (σ_x) of localization obtained by ANN (9.7 ± 0.2 nm) is significantly smaller than that of MLEG (11.5 ± 0.4 nm, $P = 9.8 \times 10^{-6}$) and NLLSG (12.6 ± 0.4 nm, $P = 4.1 \times 10^{-13}$) (Fig. 4C). It is not appropriate to directly compare the average widths of actin fibers (Fig. 4D) as they might be comprised of different numbers of individual filaments. Hence, we normalized each fiber according to the value obtained by ANN and found that the full width at half maximum (FWHM) obtained by ANN is significantly smaller than that of MLEG (1.24 ± 0.03, $P = 7.0 \times 10^{-11}$) and NLLSG (1.32 ± 0.04, $P = 1.4 \times 10^{-13}$) (Fig. 4E). Since the ground truth of the widths of actin fibers were unknown, we further imaged spin-coated λ-DNA with PicoGreen (Fig. 4F and 4G), employing a so-called binding-activated localization microscopy (BALM) (Schoen et al., 2011). We found that the FWHM of DNA obtained by ANN (20.7 ± 1.2 nm) (Fig. 4H) is significantly smaller than that of MLEG (26.2 ± 1.3 nm, $P = 0.0077$) and NLLSG (29.3 ± 1.0 nm, $P = 0.000036$) (Fig. 4I).

Extension of ANN to 3D imaging

ANN can be easily extended to three-dimensional (3D) super-resolution imaging by training with defocused PSFs (Fig. S4). To achieve higher precision, ANN should be applied in conjunction with biplane microscopy (Juette et al., 2008), where PSFs at two planes are used for training (Fig. 5A). To test the performance of ANN in real 3D imaging experiments, we have employed biplane STORM imaging of microtubules labeled with Alexa Fluor 647 in COS-7 cells (Fig. 5B and 5C). We achieved a position precision of 9 nm, 10 nm, and 21 nm in *x*, *y*, *z* axis, respectively, consistent with our simulation results (Fig. S6).

DISCUSSION

Besides the accuracy and precision, ANN takes much less time to determine the localization. For fitting algorithms, a function (either Gaussian or PSF) has to be generated, and a criterion (sum of error squares or log-likelihood) has to be calculated for each iteration. Then a strategy has to be employed to converge the fitting for multiple iterations. Apparently,

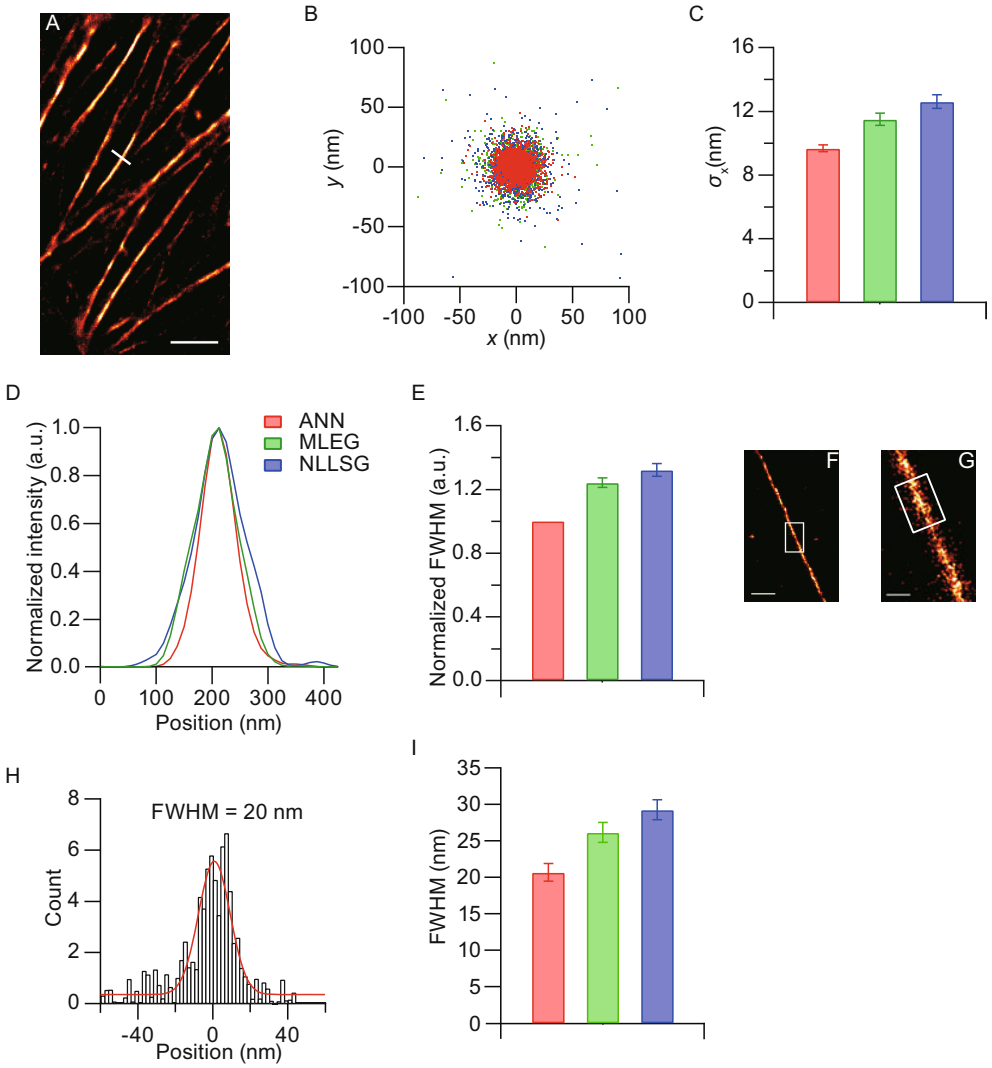

Figure 4. Evaluating the performance of ANN in PALM and BALM experiments. (A) PALM image of HeLa cell expressing Lifeact fused with mEos2. (B) Localization distributions of mEos2 molecules obtained by ANN, MLEG and NLLSG. Localizations from 261 molecules (each containing >5 localizations) were aligned by their center of mass. (C) Histograms of distribution in *x* were fit to Gaussian functions. The standard deviation in *x* direction (σ_x) of the distribution obtained by the three algorithms were 9.7 ± 0.2 nm, 11.5 ± 0.4 nm and 12.6 ± 0.4 nm, respectively. (D) The normalized fluorescence intensity across the line in (A). (E) The normalized FWHM of actin fibers obtained by the three algorithms were 1, 1.24 ± 0.03 and 1.32 ± 0.04, respectively (n = 40). (F) Reconstructed image of spin-coated λ-DNA recorded with PicoGreen. (G) The magnified images of the rectangle region in (F). (H) Line profile of the rectangle region in (G) for determining the FWHM of DNA. The analyzed segment length was 200 nm. (I) The FWHM of DNA obtained by the three algorithms were 20.7 ± 1.2 nm, 26.2 ± 1.3 nm and 29.3 ± 1.0 nm, respectively (n = 10). The scale bars are 2 μm (A), 500 nm (F) and 100 nm (G). *P* values were determined using a paired Student's *t*-test, and all significant statistics were compared to ANN. The error bars are ± s.e.m.

every step contributes to the speed of fitting algorithms. For ANN, PSF calculation is done for once and the image stacks generated can be used for training thereafter. After training for a specific setup, the position and orientation can be estimated independently in a fast and straightforward manner by inputting recorded images into ANN. This may explain why ANN is 1×10^5 and 5×10^3 faster than MLEwT and NLLSG, respectively (Table S1). ANN implemented with a central processing unit (CPU) is two times faster than MLEG with a graphic processing unit (GPU) implementation (Table S1), making it well suited for real time analysis.

Here, we derived the PSF of dipoles with restricted mobility and developed an ANN-based algorithm for estimating the *x*-*y*-*z* position, orientation and mobility of individual dipoles. In contrast to fitting and optimization of current single molecule localization algorithms, the core of the ANN is learning and prediction, which is more robust, efficient and adaptive. As we and others (Enderlein et al., 2006; Stallinga and Rieger,

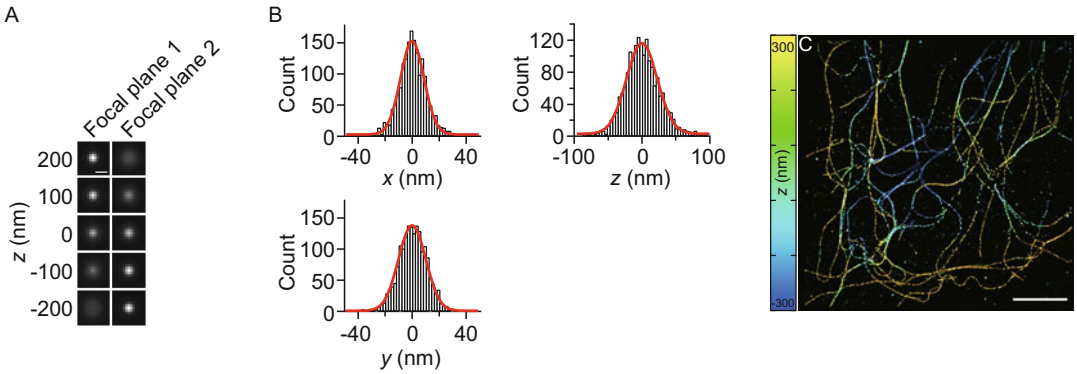

Figure 5. Evaluating the performance of ANN in biplane STORM experiments. (A) Example images of a free dipole from the two focal planes at different *z* positions. (B) Localizations from 117 Alexa Fluor 647 molecules (each containing >10 localizations) were aligned by their center of mass. Histograms of the distributions were fit to Gaussian functions, yielding standard deviations of 9 nm in *x*, 10 nm in *y* and 21 nm in *z*. The photons are about 700 ± 360 (mean ± s.d.) per frame. (C) Biplane STORM image of microtubules labeled with Alexa Fluor 647 in COS-7 cell, with the *z*–position information color-coded according to the color scale bar. Scale bars are 500 nm (A) and 5 μm (C).

2010; Engelhardt et al., 2011) have demonstrated, the most frequently used Gaussian-based fitting algorithms cannot handle the systematic error caused by tilted molecules. This systematic error can become a substantial limiting factor to obtain molecular-scale resolution. Fitting with PSFs, either simulated (MLEwT) or measured (PR-MLE) (Quirin et al., 2012), can maximally alleviate this systematic error but is impractical due to its 1×10^5 times slowness (Table S1) and low rate of convergence in real experiments (Fig. S3). Furthermore, it is impractical to measure PSFs of emitters of various orientations because a full coverage of all the angle combinations could be difficult to achieve, thus currently PR-MLE was only applied to isotropic cases. The same argument exists for biplane fitting algorithms where the increase of fitting parameters and fitting with more complicated 3D PSFs exacerbate the problem of slowness and convergence. Other than developing more accurate algorithms, one can also extract the orientation information by clever hardware engineering, i.e., excitation and/or emission with multiple polarizations (Ha et al., 1999), or double-helix PSF (DH-PSF) microscopy (Backlund et al., 2012). The hardware solutions require sophisticated hardware configurations and are usually more time-consuming, limiting their wide application. Hence, our ANN estimator based on PSF should be considered as an optimal choice for both 2D and 3D localization microscopy (Table S2).

MATERIALS AND METHODS

Plasmids construction

To generate pmEos2-C1, cDNAs of mEos2 (Addgene plasmid #20341) containing NheI and BglII sites were PCR-amplified and swapped with the EGFP gene in the pEGFP-C1 vector (Clontech). To express Lifeact fused fluorescent proteins in mammalian cells, the Lifeact sequence was cloned into pEGFP-N1 (Clonetech) with *Eco*RI and *Bam*HI. Then, mEos2 containing *Bam*HI and *Not*I sites were PCR-amplified and inserted into the plasmid instead of EGFP. The synthetic DNA primers used for cloning were purchased from Invitrogen. All plasmids were sequenced (The Beijing Genomics Institute) before further analysis.

Cell culture, transfection and fixation

COS-7 and HeLa cells were cultured in DMEM complete medium (Gibco) supplemented with 10% fetal bovine serum and maintained at 37°C and 5% CO_2 in a humidified incubator (Thermo). The cells were then transiently transfected using Lipofectamine™ 2000 (Invitrogen) in accordance with the manufacturer's protocol. After transfection, the cells were grown in IMEM or DMEM complete medium (Gibco) without phenol red for 24 h. For fixed cell imaging, the cells were re-cultured on coverslips (Fisher Scientific) for another 24 h and then fixed with 3% (*w/v*) paraformaldehyde and 0.5% glutaraldehyde in PBS for 15–40 min at 37°C, washed 3–5 times with filtered PBS and stored in PBS until imaging.

DNA preparation

The protocol of BALM sample preparation and imaging were performed as described before (Schoen et al., 2011). Cleaned coverslips were first treated with 0.1 g/L poly-L-lysine (Sigma) for 1 h, washed twice and then blown dry. DNA from lambda phage were purchased from Takara and diluted to a concentration of 0.34 mg/L in the standard imaging buffer (TE50), which contained 50 mmol/L Tris-HCl, 50 mmol/L NaCl, 1 mmol/L EDTA, pH 7.5. The 80 μL of diluted DNA was added on poly-L-lysine coated coverslip using a spin-coater at a rotation speed of 3000 rpm. Then the coverslip was washed with 4 mL of ddH_2O. The BALM imaging buffer contained 10 mmol/L ascorbic acid, 1 mmol/L methyl viologen and 150 pmol/L PicoGreen (Invitrogen) diluted in TE buffer.

Immunofluorescence staining of microtubules for biplane STORM imaging

Fixed COS-7 cells were permeabilized for 10 min with 0.1% Triton X-100 and then blocked in 5% bovine serum albumin (BSA, AMRESCO) diluted PBS for 60 min. The mouse anti-β tubulin monoclonal

antibody (Sungene biotech) was diluted 1:200 in 2.5% BSA diluted PBS and added on COS-7 cells in 37°C incubator for 60 min. After three times rinsing with PBS, COS-7 cells were then incubated for another 60 min with Alexa Fluor 647 labeled rabbit anti-mouse secondary antibody (Invitrogen) which was also 1:200 diluted in PBS. At last, the cells were rinsed four times with PBS and kept in dark place. The STORM imaging buffer contained imaging buffer base (10% glucose (*m/v*), 50 mmol/L Tris (pH 8.0) and 10 mmol/L NaCl), an oxygen scavenger system (0.5 mg/mL glucose oxidase (Sigma-Aldrich), 40 μg/mL catalase (Sigma-Aldrich)) and 10 mmol/L MEA.

Optical setup and imaging

PALM imaging of mEos2 and BALM imaging of DNA were performed as previously described (Betzig et al., 2006; Schoen et al., 2011). We used an Olympus IX71 inverted microscope equipped with a 100 × 1.45 numerical aperture (NA) oil objective (Olympus PLAN APO). An internal 1.6× magnification was used to yield a pixel size of 100 nm (mEos2). Alternatively, a 150 × 1.45 NA oil objective (Olympus UAPO) was used without the internal magnification (PicoGreen and Alexa Fluor 647). Four lasers (405 nm (OBIS, Coherent), 488 nm (Sapphire, Coherent), 561 nm (Sapphire, Coherent) and 647 nm (OBIS, Coherent) were controlled by an acousto-optic tunable filter (AA Optoelectronic). For excitation, the powers of 488 nm (PicoGreen), 561 nm (mEos2) and 647 nm (Alexa Fluor 647) lasers were 20.01 mW, 8.74 mW and 29.71 mW, respectively, measured near the rear pupil of the objective. The intensity of 405 nm laser, typically 10–30 μW, was adjusted so that a low density of molecules (mEos2 and Alexa Fluor 647) was activated at each frame. A λ/4 plate was used to produce circular polarization excitation light. The fluorescence signals were acquired using an electron-multiplying charge-coupled device (EMCCD) camera (Andor iXon DU-897). The biplane system was similar as previous study (Juette et al., 2008). A 50:50 beam splitter was used to generate two beam paths with a separation of 500 nm. The two light paths were separately projected onto two different areas of the same camera. The images were acquired at a frame rate of 10 Hz (mEos2), 20 Hz (PicoGreen) and 50 Hz (Alexa Fluor 647), respectively. The EM gain of EMCCD was set to 300 for all the imaging. The data analysis and super-resolution image reconstruction was performed as previously described (Zhang et al., 2012). In order to minimize the influence of the background, TIRF (total internal reflection) or near TIRF (for defocused and 3D imaging) illumination was used in this study.

Imaging of fluorescent beads

50 μL (1:10,000 diluted in H_2O) of 20-nm fluorescent beads (FluoSpheres, 580/605; Invitrogen) were deposited on the top surface of a coverslip and blow-dried with purified air. The sample was photobleached for several minutes to avoid saturation before acquisition with the same setup as that used for PALM imaging.

Q rods imaging

The Q rods (a gift from Toshio Yanagida) were diluted in PBS buffer containing BSA (1 mg/mL) at a concentration of 0.1 μmol/L. Then the Q rods were diluted to 0.05 nmol/L in Tris-HCl (pH = 7.0). To immobilize the Q rods, 30 μL of diluted solution with 0.1 μm TetraSpeck microspheres (Invitrogen) (used for z-position correction) was mixed with 27.5 μL of acrylamide, 0.75 μL of 10% TEMED and 0.75 μL of 10% ammonium persulfate. The reaction occurred in a 200 μL eppendorf tube. After polymerization, the samples were cut into thin slices from different directions to obtain Q rods with different tilt angles. Finally, the immobilized Q rods were imaged using PALM microscopy as previously described. A 150 × 1.45 NA oil objective (Olympus UAPO) was used with a 1.6× internal magnification, making a pixel size of 67 nm. The images were acquired at a frame rate of 20 Hz.

Synthetic data generation

We generated images for training data according to the theoretical PSF of each case. The center position of each simulated image is uniformly distributed within the central pixel (± 1 pixel for defocused and 3D images) to prevent a biased result. All images were generated in 7 × 7 pixels (9 × 9 pixels for defocused and 3D images) with a pixel size of 100 nm, the same as that used for experimental data. Next, the stack of images was corrupted with both shot (Poisson) noise and read out (Gaussian) noise. To mimic the real situation, we added Poisson noise according to the gain and conversion factor (to convert counts to photoelectrons, 10.5 electrons per A/D count at unity gain) of EMCCD and Gaussian noise by calculating the background noise of real images. In this paper, we used a gain of 300 for single molecule detection and fluorescent beads imaging, and the Gaussian background noise was approximately 1.5 photons/pixel (the constant background is about 5 photons) for both situations.

ANN training and simulation

Different training algorithms exist, and the selection of the most appropriate one for a given problem depends on many factors, including the complexity of the problem, the number of data points in the training set, the number of weights and biases in the network, the error goal, and whether the network is being used for pattern recognition or function approximation. First, we tested nine commonly used training functions implemented in Matlab (R2010a, 64-bit, MathWorks) and found 'trainlm' to be the best for our purpose. Then, the important parameters of ANN training, such as the structure of hidden layers and the size of the training data, were carefully tested and adjusted with synthetic data. The generation of the training data for ANN is almost the same as above, except the photons were uniformly distributed from 10 to 10,000 to cover the photons detected from different fluorescent molecules. ANN can produce satisfactory results regardless of the photon distribution of testing data. For fixed dipole, the azimuthal angle φ and polar angle θ were uniformly distributed between 0–360° and 0–90°, respectively. For restricted dipole, the half cone angle δ were uniformly distributed from 0° to 90°. We generated 100,000 images for the training of ANN in the case of perfect focus (z = 0). For the defocused analysis, 400,000 images were generated with z values randomly distributed within ± 300 nm. The precision of defocused analysis could be further increased by increasing the number of training images, but this will require much longer time and larger memory size (>32 GB). For ANN-based biplane estimation, 400,000 pairs of images from the two focal planes (with a separation of 500 nm) were generated as training data. Afterwards, the trained ANN was used to estimate the z position and obtain the position error.

MLEG, NLLSG and MLEwT

We used the GPU-based MLEG algorithm for comparison because

it is the fastest method currently available. We used 'lsqcurvefit', an existing implementation of Matlab, to do the standard 2D Gaussian fitting. The C implementation would be much faster (about two orders of magnitude) (Smith et al., 2010). We tested on two computers with different configurations (Table S1). Only one thread of CPU was used for ANN and NLLSG because we did not enable the multithreading in Matlab. For free and fixed dipole cases, Python codes of MLEwT were used for the comparison. For restricted dipole, we implemented the codes of MLEwT for restricted mobility in Matlab and compared it with ANN. The program of ANN can be found here (http://super-resolution.cn/).

ACKNOWLEDGEMENTS

We thank L. L. Looger (Janelia Farm Research Campus) for providing the mEos2 cDNA and Toshio Yanagida (Osaka University, Japan) for sharing the Q rods. This work was supported by grants from the National Basic Research Program (973 Program) (Nos. 2010CB833701 and 2010CB912303), the National Key Technology R&D Program (SQ2011SF11B01041), the National Natural Science Foundation of China (Grant Nos. 31130065, 31170818, 90913022, 31127901, and 31100615), the Beijing Natural Science Foundation (7121008), the Chinese Academy of Sciences Project (KSCX1-1W-J-3, KSCX2-EW-Q-11, and 2009-154-27).

ABBREVIATIONS

ANNs, artificial neural networks; CPU, central processing unit; GPU, graphic processing unit; MLE, maximum likelihood estimation; NLLS, nonlinear least-squares; PALM, photoactivated localization microscopy; PSF, point spread function

COMPLIANCE WITH ETHIC GUIDELINES

Yongdeng Zhang, Lusheng Gu, Hao Chang, Wei Ji, Yan Chen, Mingshu Zhang, Lu Yang, Bei Liu, Liangyi Chen, and Tao Xu declare that they have no conflict of interest.

This article does not contain any studies with human or animal subjects performed by the any of the authors.

REFERENCES

Aquino, D., Schonle, A., Geisler, C., Middendorff, C.V., Wurm, C.A., Okamura, Y., Lang, T., Hell, S.W., and Egner, A. (2011). Two-color nanoscopy of three-dimensional volumes by 4Pi detection of stochastically switched fluorophores. Nat Methods 8, 353–359.

Backlund, M.P., Lew, M.D., Backer, A.S., Sahl, S.J., Grover, G., Agrawal, A., Piestun, R., and Moerner, W.E. (2012). Simultaneous, accurate measurement of the 3D position and orientation of single molecules. Proc Natl Acad Sci U S A 109, 19087–19092.

Betzig, E., Patterson, G.H., Sougrat, R., Lindwasser, O.W., Olenych, S., Bonifacino, J.S., Davidson, M.W., Lippincott-Schwartz, J., and Hess, H.F. (2006). Imaging intracellular fluorescent proteins at nanometer resolution. Science 313, 1642–1645.

Born, M., and Wolf, E. (1999). Principles of optics: electromagnetic theory of propagation, interference and diffraction of light, 7th expanded edn (Cambridge; New York, Cambridge University Press).

Cartwright, H.M. (2008). Artificial neural networks in biology and chemistry: the evolution of a new analytical tool. Methods Mol Biol 458, 1–13.

Chang, H., Zhang, M., Ji, W., Chen, J., Zhang, Y., Liu, B., Lu, J., Zhang, J., Xu, P., and Xu, T. (2012). A unique series of reversibly switchable fluorescent proteins with beneficial properties for various applications. Proc Natl Acad Sci U S A 109, 4455–4460.

Dale, R.E., Hopkins, S.C., an der Heide, U.A., Marszalek, T., Irving, M., and Goldman, Y.E. (1999). Model-independent analysis of the orientation of fluorescent probes with restricted mobility in muscle fibers. Biophys J 76, 1606–1618.

Enderlein, J., Toprak, E., and Selvin, P.R. (2006). Polarization effect on position accuracy of fluorophore localization. Opt Express 14, 8111–8120.

Engelhardt, J., Keller, J., Hoyer, P., Reuss, M., Staudt, T., and Hell, S.W. (2011). Molecular orientation affects localization accuracy in superresolution far-field fluorescence microscopy. Nano Lett 11, 209–213.

Ha, T., Laurence, T.A., Chemla, D.S., and Weiss, S. (1999). Polarization spectroscopy of single fluorescent molecules. Phy Chem 103, 6839–6850.

Hess, S.T., Girirajan, T.P., and Mason, M.D. (2006). Ultra-high resolution imaging by fluorescence photoactivation localization microscopy. Biophys J 91, 4258–4272.

Irving, M. (1996). Steady-state polarization from cylindrically symmetric fluorophores undergoing rapid restricted motion. Biophys J 70, 1830–1835.

Juette, M.F., Gould, T.J., Lessard, M.D., Mlodzianoski, M.J., Nagpure, B.S., Bennett, B.T., Hess, S.T., and Bewersdorf, J. (2008). Three-dimensional sub-100 nm resolution fluorescence microscopy of thick samples. Nat Methods 5, 527–529.

McKinney, S.A., Murphy, C.S., Hazelwood, K.L., Davidson, M.W., and Looger, L.L. (2009). A bright and photostable photoconvertible fluorescent protein. Nat Methods 6, 131–133.

Mortensen, K.I., Churchman, L.S., Spudich, J.A., and Flyvbjerg, H. (2010). Optimized localization analysis for single-molecule tracking and super-resolution microscopy. Nat Methods 7, 377–381.

Ober, R.J., Ram, S., and Ward, E.S. (2004). Localization accuracy in single-molecule microscopy. Biophys J 86, 1185–1200.

Ohmachi, M., Komori, Y., Iwane, A.H., Fujii, F., Jin, T., and Yanagida, T. (2012). Fluorescence microscopy for simultaneous observation of 3D orientation and movement and its application to quantum rod-tagged myosin V. Proc Natl Acad Sci U S A 109, 5294–5298.

Quirin, S., Pavani, S.R., and Piestun, R. (2012). Optimal 3D single-molecule localization for superresolution microscopy with aberrations and engineered point spread functions. Proc Natl Acad Sci U S A 109, 675–679.

Riedl, J., Crevenna, A.H., Kessenbrock, K., Yu, J.H., Neukirchen, D., Bista, M., Bradke, F., Jenne, D., Holak, T.A., Werb, Z., et al. (2008). Lifeact: a versatile marker to visualize F-actin. Nat Methods 5, 605–607.

Rust, M.J., Bates, M., and Zhuang, X. (2006). Sub-diffraction-limit imaging by stochastic optical reconstruction microscopy (STORM). Nat Methods 3, 793–795.

Schoen, I., Ries, J., Klotzsch, E., Ewers, H., and Vogel, V. (2011). Binding-activated localization microscopy of DNA structures. Nano Lett 11, 4008–4011.

Shtengel, G., Galbraith, J.A., Galbraith, C.G., Lippincott-Schwartz, J., Gillette, J.M., Manley, S., Sougrat, R., Waterman, C.M., Kanchana-

wong, P., Davidson, M.W., et al. (2009). Interferometric fluorescent super-resolution microscopy resolves 3D cellular ultrastructure. Proc Natl Acad Sci U S A 106, 3125–3130.

Smith, C.S., Joseph, N., Rieger, B., and Lidke, K.A. (2010). Fast, single-molecule localization that achieves theoretically minimum uncertainty. Nat Methods 7, 373–375.

Stallinga, S., and Rieger, B. (2010). Accuracy of the Gaussian Point Spread Function model in 2D localization microscopy. Opt Express 18, 24461–24476.

Testa, I., Schonle, A., von Middendorff, C., Geisler, C., Medda, R., Wurm, C.A., Stiel, A.C., Jakobs, S., Bossi, M., Eggeling, C., et al. (2008). Nanoscale separation of molecular species based on their rotational mobility. Opt Express 16, 21093–21104.

Thompson, R.E., Larson, D.R., and Webb, W.W. (2002). Precise nanometer localization analysis for individual fluorescent probes. Biophys J 82, 2775–2783.

Zhang, M., Chang, H., Zhang, Y., Yu, J., Wu, L., Ji, W., Chen, J., Liu, B., Lu, J., Liu, Y., et al. (2012). Rational design of true monomeric and bright photoactivatable fluorescent proteins. Nat Methods 9, 727–729.